Journal of Sound and Vibration 331 (2012) 3544–3557

Contents lists available at SciVerse ScienceDirect

Journal of Sound and Vibration

journal homepage: www.elsevier.com/locate/jsvi

Forced motion and acoustic radiation of an elastic cylinder in axial flow

A. Manela [a,*], T. Miloh [b]

[a] Faculty of Aerospace Engineering, Technion – Israel Institute of Technology, Haifa 32000, Israel
[b] School of Mechanical Engineering, Tel Aviv University, Ramat Aviv 69978, Israel

ARTICLE INFO

Article history:
Received 18 October 2011
Received in revised form
20 March 2012
Accepted 21 March 2012
Handling Editor: L. Huang
Available online 10 April 2012

ABSTRACT

We study the forced motion and far-field acoustic radiation of an elastic cylinder subject to uniform axial flow and actuated at its upstream end by small-amplitude periodic displacement and rotation. The linearized problem is analysed under subcritical conditions of low nondimensional stream-flow velocity, $u < u_{cr}$, where the unforced cylinder is aligned with the external flow. It is found that the forced motion at subcritical conditions is affected by the properties of the *in vacuo* system. A resonance is excited when the cylinder is actuated at one of its *in vacuo* eigenfrequencies, ω_{res}, manifested by relatively large deflections. Fluid flow acts to regularize this behavior by transferring energy from the upstream driver to the fluid. The dynamical description is used as a source term in the formulation of the vibroacoustic problem. Assuming the cylinder is well-streamlined and neglecting the effect of vortex shedding, the far field sound is attributed directly to cylinder vibration. Acoustic radiation of a dipole type is found in the limit where the cylinder is acoustically compact. Following the dynamical description, it is shown that fluid flow reduces the sound level compared to that in the absence of mean flow, when actuation is applied close to $\omega = \omega_{res}$. In addition, we demonstrate that far-field sound can be controlled by varying the actuation parameters. Analytical description of the dynamical and acoustic fields is obtained in the limit $u \ll 1$, and found in close agreement with the exact numerical solution up to $u \sim O(1)$. Discrepancies between the approximate and exact solutions are observed close to the resonance frequencies, and rationalized in terms of the strong fluid–structure coupling occurring when $\omega \to \omega_{res}$. At $\omega = \omega_{res}$, a qualitative description of the effect of fluid stream flow on the system behavior is supplied.

1. Introduction

Fluid–structure interactions of elastic bodies are ubiquitous phenomena, common in numerous natural environments as well as engineering applications [1,2]. One fundamental setup which has been studied extensively over the years consists of a flexible cylinder, fixed at its upstream end, and free at its downstream end, subject to uniform mean flow parallel to its axis. In this setup, transverse body motions can be induced by either fluidelastic instability of the cylinder or external excitation applied to the structure. The latter may result from surrounding flow non-uniformities (e.g., sudden gust or incident turbulence), or forced vibrations transmitted (accidentally or in purpose) to the cylinder. In practical

* Corresponding author. Tel.: +972 48292237; fax: +972 48292030.
E-mail address: avshalom@aerodyne.technion.ac.il (A. Manela).

0022-460X/$ - see front matter © 2012 Elsevier Ltd. All rights reserved.
http://dx.doi.org/10.1016/j.jsv.2012.03.021

applications, excessive departures of the cylinder from its initial straight-line form may cause various unwarranted phenomena, including structural fatigue and buckling, as well as flow separation and increased aerodynamic drag.

Existing works on the dynamics of elastic cylinders in axial flow focus on the case of unforced motion, thus disregard the effect of external excitation on structure dynamics. Consequently, the linearized problem is formulated as an eigenvalue problem for the fluidelastic instability of the reference straight state, and the critical conditions for the onset of instability are investigated. Non-linear analyses then consider the cylinder motion at supercritical conditions. In a series of works, Païdoussis and co-workers [2–5] have shown that when the cylinder is sufficiently streamlined, system instability takes place initially by divergence (in the form of a standing wave), and then, with increasing flow velocity, by flutter. Triantafyllou and Chryssostomidis [6] derived an analytic description for the onset of buckling of a slender cylinder. Dowling [7] considered cylinders with small bending rigidity, and studied the unforced and forced (see below) problems using matched asymptotic expansion. Bending stiffness was taken into account only in the vicinity of a critical point, where the effect of tension in the cylinder is canceled. Other works studied the effect of cylinder length on the instability, in cases where the system tension force is driven by gravity or friction [8–10].

In physical applications, external forcing of the system may be inevitable through fluid–structure interactions of the cylinder with incident non-uniformities in the flow, or random vibrations transferred to the structure at its upstream end. It is therefore of practical importance to analyse these situations. Mathematically, the set of problems to be solved in such scenarios is qualitatively different than in the unforced case: instead of searching for a non-trivial eigenvalue solution, a particular solution satisfying the actual form of external forcing needs to be found. In an effort to model the biofluidic mechanism of small-scale flapping flight, recent theoretical works have examined the coupling between structure elasticity, fluid flow and external forcing, by focusing on the motion of a thin flexible wing driven by leading edge pitching and heaving [11,12]. To the best of our knowledge, the counterpart problem for an elastic cylinder has been considered only in Ref. [7], where the cylinder response to harmonic displacement has been studied in the limit of infinitely small structure stiffness. We further elaborate on the analysis in Ref. [7], in light of the present work, in Section 4.

The *vibroacoustic* problem, namely the calculation of sound produced by the interaction between structure elasticity and surrounding flow, has been studied in different setups to examine the effect of elasticity as a mean for noise reduction. Previous works have focused on the scattering of sound from interaction of elastic plates with uniform steady [13] and unsteady [14] flows. Recently, the acoustic radiation of a thin elastic plate, actuated at its leading edge, has been analysed [15]. Yet, no study has considered the vibroacoustic problem for an elastic cylinder. Apart from its fundamental significance, such analysis may be useful as a preliminary tool for the identification and characterization of forced deformations in axisymmetric elastic configurations, such as underwater towed sonar arrays or aerial windsocks. It may therefore prove beneficial as a mean for motion detection from afar.

The primary objective of the present work is to investigate the forced motion and far-field acoustic signature of an elastic cylinder actuated at its upstream end. Towards this end, we consider a linearized problem, where both upstream-end translation and rotation are prescribed, and analyze the forced motion in the transverse direction. The analysis is then applied to predict the far-field acoustic radiation, taking into account the structure dynamics as a sound source term. We focus on the case of sinusoidal actuation, and consider subcritical conditions where the unforced cylinder does not deflect. This last assumption assures consistency with our outset linear-theory assumption; analysis of the non-linear problem is left for later contributions.

The paper outline is as follows: in Section 2, both dynamical and acoustic problems are formulated for the case of sinusoidal upstream-end actuation. In Section 3, the problems are analysed and numerical results are presented. Both numerical solution and analytic approximations are presented and compared. A summary of our findings and concluding comments is given in Section 4.

2. Problem formulation

2.1. Dynamical problem

Consider an elastic cylinder of radius a, length L, and mass m per unit length, towed in a fluid of mean density ρ_0 (Fig. 1). The cylinder is subject to outer low-Mach number uniform stream flow of speed U in the X_1-direction (parallel to the undisturbed position of the cylinder axis), as well as to time-dependent leading edge displacement, $\mathrm{L}\varepsilon_\mathrm{d}\Phi(\mathrm{T})$, and rotation, $\varepsilon_\mathrm{r}\Psi(\mathrm{T})$, in the transverse X_2 and normal X_3 directions, respectively. To focus on the case of linearized motion, both ε_d and ε_r are assumed small. In addition, we consider a slender cylinder ($\mathrm{a/L} \ll 1$), modeled as an elastic beam, with its motion fully described by the location of its symmetry axis. The cylinder is located between $\mathrm{X}_1 = -\mathrm{L}$ (upstream actuated end) and $\mathrm{X}_1 = 0$ (downstream free end).

Under the above assumptions, small-amplitude unsteady deflections of the cylinder in the X_2-direction of amplitude $\xi(\mathrm{X}_1,\mathrm{T}) \ll \mathrm{L}$ are taken to satisfy the linearized equation [2]

$$\mathrm{m}\frac{\partial^2\xi}{\partial \mathrm{T}^2} + \mathrm{B}\frac{\partial^4\xi}{\partial \mathrm{X}_1^4} - \frac{\partial}{\partial \mathrm{X}_1}\left(\Theta\frac{\partial\xi}{\partial \mathrm{X}_1}\right) = \mathrm{F_f}, \tag{1}$$

where $B=EI$ is the cylinder bending stiffness (E being Young's modulus and I is the moment of inertia), $\Theta(\mathrm{X}_1)$ is the axial tension (see (6)), and $\mathrm{F_f}(\mathrm{X}_1,\mathrm{T})$ is the magnitude of the transverse fluid force acting on the cylinder per unit length. The fluid

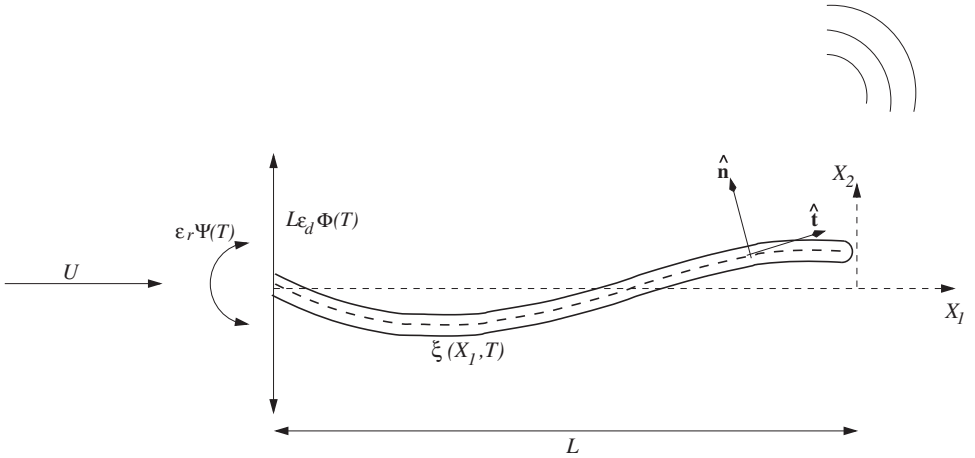

Fig. 1. Schematic of the problem: a long elastic cylinder of length L is subject to axial flow of speed U, and its upstream end is actuated at prescribed small-amplitude time-dependent displacement $\mathrm{L}\varepsilon_d\Phi(\mathrm{T})$ and rotation $\varepsilon_r\Psi(\mathrm{T})$.

loading vector force acting along the cylinder per unit length is given by the sum of an inviscid force [16]

$$\mathbf{F_A} = -\rho_0 \mathrm{A}\left(\frac{\partial}{\partial \mathrm{T}} + \mathrm{U}\frac{\partial}{\partial \mathrm{X}_1}\right)^2 \xi\, \hat{\mathbf{x}}_2, \tag{2}$$

where $\mathrm{A} = \pi \mathrm{a}^2$ is the cylinder cross-sectional area and $\hat{\mathbf{x}}_2$ is a unit vector in the transverse direction; and a viscous drag force with normal

$$\mathbf{F_N} = -\rho_0 \mathrm{aUC_N}\left(\frac{\partial}{\partial \mathrm{T}} + \mathrm{U}\frac{\partial}{\partial \mathrm{X}_1}\right)\xi \hat{\mathbf{n}} \tag{3}$$

and tangential

$$\mathbf{F_T} = \rho_0 \mathrm{aU}^2 \mathrm{C_T}\hat{\mathbf{t}} \tag{4}$$

force components, where $\hat{\mathbf{n}}$ and $\hat{\mathbf{t}}$ are local normal and tangential unit vectors along the cylinder, respectively, and C_N and C_T are the respective drag coefficients [2]. Projecting the forces in (2)–(4) onto the transverse direction, we find

$$\mathrm{F_f} = -\rho_0 \mathrm{a}\left[\mathrm{U}^2(\mathrm{C_N} - \mathrm{C_T})\frac{\partial}{\partial \mathrm{X}_1} + \mathrm{UC_N}\frac{\partial}{\partial \mathrm{T}} + 2\pi \mathrm{Ua}\frac{\partial^2}{\partial \mathrm{X}_1 \partial \mathrm{T}} + \pi \mathrm{a}\frac{\partial^2}{\partial \mathrm{T}^2}\right]\xi, \tag{5}$$

where the contribution from the centrifugal load (the $\partial^2\xi/\partial \mathrm{X}_1^2$ term in (2)) has been omitted and will be included in the tension term for convenience. The tension $\Theta(\mathrm{X}_1)$ is subsequently given by the linearly varying distribution

$$\Theta(\mathrm{X}_1) = -\rho_0 \mathrm{aU}^2(\pi \mathrm{a} - 2\mathrm{aC_b} + \mathrm{C_T X}_1), \tag{6}$$

resulting from the centrifugal load omitted in (5) (the first term on the RHS of (6)), and a boundary layer drag-induced force acting on the cylinder (the other two terms on the RHS of (6)). Here C_b denotes a base drag force coefficient, characterizing the fluid loading acting at the free end of the cylinder [2]. Substituting (5) and (6) into (1) and rearranging, yields

$$(\mathrm{m} + \rho_0 \mathrm{A})\frac{\partial^2 \xi}{\partial \mathrm{T}^2} + \mathrm{B}\frac{\partial^4 \xi}{\partial \mathrm{X}_1^4} - \Theta(\mathrm{X}_1)\frac{\partial^2 \xi}{\partial \mathrm{X}_1^2} + 2\rho_0 \mathrm{UA}\frac{\partial^2 \xi}{\partial \mathrm{X}_1 \partial \mathrm{T}} + \rho_0 \mathrm{aU}^2 \mathrm{C_N}\frac{\partial \xi}{\partial \mathrm{X}_1} + \rho_0 \mathrm{aUC_N}\frac{\partial \xi}{\partial \mathrm{T}} = 0. \tag{7}$$

The dynamical problem is complemented by four boundary conditions, specifying the cylinder displacement and rotation at the upstream end $\mathrm{X}_1 = -\mathrm{L}$

$$\xi(-\mathrm{L}) = \varepsilon_\mathrm{d} \mathrm{L}\Phi(\mathrm{T}), \quad \left.\frac{\partial \xi}{\partial \mathrm{X}_1}\right|_{-\mathrm{L}} = \varepsilon_\mathrm{r}\Psi(\mathrm{T}), \tag{8}$$

and imposing zero moment and a fluid–structure force balance at the downstream end $\mathrm{X}_1 = 0$

$$\left.\frac{\partial^2 \xi}{\partial \mathrm{X}_1^2}\right|_0 = \left[\mathrm{EI}\frac{\partial^3 \xi}{\partial \mathrm{X}_1^3} + \mathrm{f}\rho_0 \mathrm{AU}\left(\frac{\partial \xi}{\partial \mathrm{T}} + \mathrm{U}\frac{\partial \xi}{\partial \mathrm{X}_1}\right)\right]_0 = 0. \tag{9}$$

The parameter f depends on the shape of the downstream end, and varies between zero (for a blunt end) and unity (for a perfectly streamlined end) [2]. Typical values of the hydrodynamic coefficients appearing in (6)–(9) will be discussed in Section 3.

2.2. Acoustic field

Assuming the flow is homentropic and attached to the structure, the effect of vortex shedding is negligible, and sound generation is attributed directly to the cylinder motion. In the linearized approximation, the acoustic pressure is given by [17,18]

$$\mathrm{P}(\mathbf{X},\mathrm{T}) = \rho_0 \frac{\partial}{\partial \mathrm{T}} \int_{-\infty}^{\infty} \oint_{\mathrm{S}} \mathrm{V_n}(\mathbf{Y},\tau)\mathrm{G}(\mathbf{X},\mathbf{Y},\mathrm{T}-\tau)\,\mathrm{dS}(\mathbf{Y})\,\mathrm{d}\tau, \tag{10}$$

where S is the surface of the cylinder, $\mathrm{V_n}(\mathbf{Y},\tau)$ its normal velocity directed into the fluid, and $\mathrm{G}(\mathbf{X},\mathbf{Y},\mathrm{T}-\tau)$ the acoustic Green's function having a vanishing normal derivative on the undisturbed cylinder.

We assume that the cylinder is acoustically compact, i.e. that $\mathrm{a}/\lambda \ll 1$, where $\lambda = 2\pi/\mathrm{k}$ is the acoustic wavelength, $\mathrm{k} = \Omega/\mathrm{c_0}$ is the dimensional acoustic wavenumber, c_0 is the speed of sound, and Ω is a frequency characterizing the cylinder motion (see Section 2.4). The condition for cylinder compactness is therefore that $\mathrm{a}/\lambda = \Omega \mathrm{a}/2\pi \mathrm{c_0} \ll 1$, and is assured by considering actuations with $\Omega \ll \mathrm{c_0}/\mathrm{a}$. We apply the compact approximation of the Green's function [18]

$$\mathrm{G}(\mathbf{X},\mathbf{Y},\mathrm{T}-\tau) = \frac{1}{4\pi|\mathbf{X}^{\mathrm{kir}}-\mathbf{Y}^{\mathrm{kir}}|}\,\delta\left(\mathrm{T}-\tau-\frac{|\mathbf{X}^{\mathrm{kir}}-\mathbf{Y}^{\mathrm{kir}}|}{\mathrm{c_0}}\right), \tag{11}$$

to evaluate the far-field acoustic radiation. Here, $\mathbf{X}^{\mathrm{kir}}(\mathbf{X})$ and $\mathbf{Y}^{\mathrm{kir}}(\mathbf{Y})$ denote the *Kirchhoff* vectors for the cylinder, whose components represent the velocity potentials of incompressible flow past the body having unit speed in the respective directions at large distances from the body. For the present finite-cylinder configuration, we approximate the Kirchhoff vector by [18]

$$\mathrm{Y}_1^{\mathrm{kir}} = \mathrm{Y}_1, \quad \mathrm{Y}_{\mathrm{j}}^{\mathrm{kir}} = \begin{cases} \mathrm{Y_j}\left(1+\dfrac{\mathrm{a}^2}{\mathrm{Y}_2^2+\mathrm{Y}_3^2}\right), & -\mathrm{L} \le \mathrm{Y}_1 \le 0 \\ \mathrm{Y_j}, & \mathrm{Y}_1 < -\mathrm{L} \text{ or } \mathrm{Y}_1 > 0 \end{cases}, \quad \mathrm{j} = 2,3. \tag{12}$$

To evaluate the far-field acoustic pressure, substitute (11) into the integral in (10) and expand to first order in $\mathbf{Y}^{\mathrm{kir}}$ as $|\mathbf{X}^{\mathrm{kir}}| \sim |\mathbf{X}| \to \infty$, to obtain

$$\mathrm{P}(\mathbf{X},\mathrm{T}) \approx \frac{\rho_0}{4\pi|\mathbf{X}|}\frac{\partial}{\partial \mathrm{T}} \oint_{\mathrm{S}} \mathrm{V_n}\left(\mathbf{Y},\mathrm{T}-\frac{|\mathbf{X}|}{\mathrm{c_0}}\right)\mathrm{dS}(\mathbf{Y}) + \frac{\rho_0 \mathrm{X_j}}{4\pi \mathrm{c_0}|\mathbf{X}|^2}\cdot\frac{\partial^2}{\partial \mathrm{T}^2}\oint_{\mathrm{S}} \mathrm{V_n}\left(\mathbf{Y},\mathrm{T}-\frac{|\mathbf{X}|}{\mathrm{c_0}}\right)\mathrm{Y}_{\mathrm{j}}^{\mathrm{kir}}(\mathbf{Y})\,\mathrm{dS}(\mathbf{Y}). \tag{13}$$

The first integral, representing a monopole, vanishes because the volume of the cylinder is assumed constant. The acoustic far-field is therefore of a dipole type, determined by the second integral. Along the cylinder surface, $\mathrm{dS} = \mathrm{a}\,\mathrm{d}\alpha\,\mathrm{dY}_1$, $\alpha = \cos^{-1}(\mathrm{Y}_2/\mathrm{a})$, $-\mathrm{L} \le \mathrm{Y}_1 \le 0$, and $0 \le \alpha \le 2\pi$. In addition

$$\mathrm{V_n}(\mathrm{Y}_1,\mathrm{T}) = \left.\frac{\mathrm{d}\xi}{\mathrm{d}\tau}\right|_{\mathrm{Y}_1,\tau} \cos\alpha.$$

Substituting the above relations together with (12) into (13) and carrying the integration with α, yield

$$\mathrm{P}(\mathbf{X},\mathrm{T}) \approx \frac{\rho_0 \mathrm{a}^2 \mathrm{X}_2}{2\mathrm{c_0}|\mathbf{X}|^2}\frac{\partial^3}{\partial \mathrm{T}^3}\int_{-\mathrm{L}}^{0} \xi(\mathrm{Y}_1,\mathrm{T}-|\mathbf{X}|/\mathrm{c_0})\,\mathrm{dY}_1. \tag{14}$$

That is, given the dynamical description of the cylinder shape $\xi(\mathrm{X}_1,\mathrm{T})$, the far-field sound is obtained through quadrature along Y_1, and subsequent cubic-order time-differentiation as specified by (14).

2.3. Dimensionless formulation

To facilitate comparison of our results with the unforced-motion analysis of Ref. [10], we follow the scaling introduced in Ref. [8] and later applied in Refs. [9,10]. The scaling is based on a length scale

$$\mathrm{L_n} = \frac{\mathrm{a}(\pi - 2\mathrm{C_b})}{\mathrm{C_T}},$$

marking the location of the "neutral point" $\mathrm{X}_{1_{\mathrm{n}}} = -\mathrm{L_n}$, where the local tension $\Theta(\mathrm{X}_1)$ in (6) vanishes. At this point the coefficient of $\partial^2\xi/\partial \mathrm{X}_1^2$ in (7) also vanishes, and the only stiffness mechanism in the equation of motion arises from flexural rigidity. The key importance of the neutral point for studying the dynamical problem has been demonstrated by Dowling [7], in cases where bending rigidity is infinitesimally small. Scaling ξ and X_1 by L_n, the time T by $\mathrm{L_n^2}\sqrt{(\mathrm{m}+\rho_0\mathrm{A})/\mathrm{EI}}$, and substituting into (7)–(9), yields the nondimensional form of the equation of motion

$$\frac{\partial^2\zeta}{\partial \mathrm{t}^2} + \frac{\partial^4\zeta}{\partial \mathrm{x}_1^4} + \mathrm{u}^2\left(1-\frac{1}{2}\mathrm{c_b}\right)\frac{\partial}{\partial \mathrm{x}_1}\left[(1+\mathrm{x}_1)\frac{\partial\zeta}{\partial \mathrm{x}_1}\right] + 2\mathrm{u}\sqrt{\mu}\frac{\partial^2\zeta}{\partial \mathrm{x}_1 \partial \mathrm{t}} + \mathrm{u}^2\left(1-\frac{1}{2}\mathrm{c_b}\right)\left(\frac{\mathrm{c_N}}{\mathrm{c_T}}-1\right)\frac{\partial\zeta}{\partial \mathrm{x}_1} + \mathrm{u}\sqrt{\mu}\left(1-\frac{1}{2}\mathrm{c_b}\right)\frac{\mathrm{c_N}}{\mathrm{c_T}}\frac{\partial\zeta}{\partial \mathrm{t}} = 0, \tag{15}$$

together with the boundary conditions

$$\zeta(-\mathrm{l})=\varepsilon_{\mathrm{d}}\Phi(\mathrm{t}),\quad \left.\frac{\partial\zeta}{\partial \mathrm{x}_1}\right|_{-\mathrm{l}}=\varepsilon_{\mathrm{r}}\Psi(\mathrm{t}),\quad \left.\frac{\partial^2\zeta}{\partial \mathrm{x}_1^2}\right|_0=\left[\frac{\partial^3\zeta}{\partial \mathrm{x}_1^3}+\mathrm{fu}\left(\sqrt{\mu}\frac{\partial\zeta}{\partial \mathrm{t}}+\mathrm{u}\frac{\partial\zeta}{\partial \mathrm{x}_1}\right)\right]_0=0. \tag{16}$$

Here ζ,x_1 and t mark the nondimensional cylinder deflection, axial coordinate and time, respectively, and the governing dimensionless parameters are

$$\mathrm{u}=\sqrt{\frac{\rho_0\mathrm{A}}{\mathrm{B}}}\mathrm{UL}_{\mathrm{n}},\quad \mu=\frac{\rho_0\mathrm{A}}{\mathrm{m}+\rho_0\mathrm{A}}\quad\text{and}\quad \mathrm{l}=\frac{\mathrm{L}}{\mathrm{L}_{\mathrm{n}}}, \tag{17}$$

marking the scaled stream velocity, mass ratio and compression length, respectively. For convenience, we use the notation $\mathrm{c_N}=4\mathrm{C_N}/\pi$,$\mathrm{c_T}=4\mathrm{C_T}/\pi$, and $\mathrm{c_b}=4\mathrm{C_b}/\pi$.

Applying the same scaling to expression (14) for the far field pressure fluctuation, we find

$$\mathrm{p}(\mathbf{x},\mathrm{t})\approx\frac{\mathrm{M}\cos\theta}{|\mathbf{x}|}\frac{\mathrm{a}^2}{2\mathrm{L}_{\mathrm{n}}^2}\frac{\mu^{3/2}}{\mathrm{u}^3}\frac{\partial^3}{\partial\mathrm{t}^3}\int_{-\mathrm{l}}^0\zeta(\mathrm{y}_1,[\mathrm{t}])\,\mathrm{d}\mathrm{y}_1, \tag{18}$$

where $\mathrm{p}=\mathrm{P}/\rho_0\mathrm{U}^2$ is the normalized pressure, $\mathrm{M}=\mathrm{U}/\mathrm{c}_0$ is the mean flow Mach number, $\cos\theta=\mathrm{X}_2/|\mathbf{X}|$ is the observer directivity, and $[\mathrm{t}]=\mathrm{t}-\mathrm{M}(\sqrt{\mu}|\mathbf{x}|/\mathrm{u})$ is the acoustic retarded time. The difference between the present expression for [t] and the commonly used notation $[\tilde{\mathrm{t}}]=\tilde{\mathrm{t}}-\mathrm{M}|\tilde{\mathbf{x}}|$ (where $\tilde{\mathrm{t}}$ and $|\tilde{\mathbf{x}}|$ are the nondimensional time and distance obtained by scaling T and $|\mathbf{X}|$ with L/U and L, respectively) results from the different scaling applied in the present formulation. This difference, however, does not have any physical significance; in an actual calculation where μ and u are fixed, the transformation from [t] to $[\tilde{\mathrm{t}}]$ can be obtained by simple manipulation.

2.4. Sinusoidal actuation

We consider the case of sinusoidal actuation, which can be viewed as a Fourier component of a more general (possibly non-periodic) actuation input. For simplicity, we assume that both displacement and rotation actuations are characterized by a common frequency ω, and are shifted by a phase angle φ. Consequently, the functions $\Phi(\mathrm{t})$ and $\Psi(\mathrm{t})$ in (16) are

$$\Phi(\mathrm{t})=\mathrm{e}^{\mathrm{i}\omega\mathrm{t}}\quad\text{and}\quad \Psi(\mathrm{t})=\mathrm{e}^{\mathrm{i}(\omega\mathrm{t}+\varphi)}, \tag{19}$$

and we seek for a solution of the form

$$\zeta(\mathrm{x}_1,\mathrm{t};\omega)=\mathrm{z}(\mathrm{x}_1;\omega)\mathrm{e}^{\mathrm{i}\omega\mathrm{t}}. \tag{20}$$

Substituting (19)–(20) into (15)-(16) yields an ordinary differential equation for z

$$\mathrm{z}''''+\mathrm{u}^2\left(1-\frac{1}{2}\mathrm{c_b}\right)(1+\mathrm{x}_1)\mathrm{z}''+\mathrm{u}\left[\left(1-\frac{1}{2}\mathrm{c_b}\right)\mathrm{u}\frac{\mathrm{c_N}}{\mathrm{c_T}}+2\mathrm{i}\omega\sqrt{\mu}\right]\mathrm{z}'+\omega\left[\mathrm{i}\sqrt{\mu}\left(1-\frac{1}{2}\mathrm{c_b}\right)\mathrm{u}\frac{\mathrm{c_N}}{\mathrm{c_T}}-\omega\right]\mathrm{z}=0, \tag{21}$$

together with boundary conditions

$$\mathrm{z}(-\mathrm{l})=\varepsilon_{\mathrm{d}},\quad \mathrm{z}(-\mathrm{l})=\varepsilon_{\mathrm{r}}\mathrm{e}^{\mathrm{i}\varphi},\quad \mathrm{z}''(0)=0,\quad \mathrm{z}'''(0)+\mathrm{i}\omega\mathrm{fu}\sqrt{\mu}\mathrm{z}(0)+\mathrm{uz}'(0)=0, \tag{22}$$

where primes denote differentiations with x_1. The boundary-value problem (21)–(22) is solved numerically by means of the Chebyshev collocation method [19] and the physical solution is obtained by taking the real part of (20). Substituting (20) into (18) and taking the time derivative yield an expression for the far field acoustic pressure

$$\mathrm{p}(\mathbf{x},\mathrm{t};\omega)\approx-\frac{\mathrm{M}\cos\theta}{|\mathbf{x}|}\frac{\mathrm{a}^2}{2\mathrm{L}_{\mathrm{n}}^2}\frac{\mu^{3/2}}{\mathrm{u}^3}\mathrm{i}\omega^3\mathrm{e}^{\mathrm{i}\omega[\mathrm{t}]}\int_{-\mathrm{l}}^0\mathrm{z}(\mathrm{y}_1)\,\mathrm{d}\mathrm{y}_1. \tag{23}$$

In the following, results for the far-field pressure are presented using the "kernel" of expression (23)

$$\Pi(\omega)\equiv\frac{\mu^{3/2}}{\mathrm{u}^3}\mathrm{i}\omega^3\int_{-\mathrm{l}}^0\mathrm{z}(\mathrm{y}_1)\,\mathrm{d}\mathrm{y}_1. \tag{24}$$

In this representation, the $|\mathbf{x}|^{-1}$ amplitude decay, as well as the dipole-directivity factor $\cos\theta$ appearing in (23), have been omitted for simplicity, but should nevertheless be recalled as characteristics of the cylinder acoustic radiation.

3. Numerical results

The problem formulated in Section 2 is governed by six nondimensional parameters (l,u,f,$\mathrm{c_b}$,$\mathrm{c_N}/\mathrm{c_T}$ and μ) in the absence of forcing, and three additional parameters (ε_{d},ε_{r} and φ) in the forced case. To simplify the presentation of results, we focus on a fixed value of the mass parameter $\mu=0.47$, which is close to neutral-buoyancy conditions ($\mu=0.5$), and assume the ratio $\mathrm{c_N}/\mathrm{c_T}$ between normal and tangential drag coefficients to be unity, where in practice it may vary between $0.5\le\mathrm{c_N}/\mathrm{c_T}\le1.5$ [2]. In addition, the parameters c_b and f characterizing the fluid loading at the cylinder downstream end are assumed linearly correlated through $\mathrm{c_b}=1-\mathrm{f}$, as suggested in Ref. [2] and applied in Ref. [10]. In accordance with our assumption of no flow detachment (essential for subsequent calculation of the acoustic far field), we consider a case of a

well-streamlined cylinder by taking $f=0.8$ ($c_b=0.2$). The effect of the parameter f on the results is therefore not studied in detail; however, our numerical calculations indicate that the cylinder motion remains qualitatively unaffected at lower values of f at the subcritical conditions considered. The remaining unfixed parameters are therefore u and l, as well as the forcing parameters ε_d,ε_r and φ.

In the following we first solve for the unforced problem and validate our numerical scheme by comparing with existing results. We then analyse the forced motion and acoustic radiation generated by sinusoidal actuation.

3.1. Unforced motion

The unforced motion, where the cylinder is subject only to axial flow, has been studied previously by several authors. In the linear regime, the analysis yields an eigenvalue problem, predicting the critical conditions for the onset of cylinder motion. In an actual experiment (numerical or in laboratory), where a cylinder is characterized by a fixed set of nondimensional parameters μ,c_b,c_N/c_T,l and f, there exists a critical value of the nondimensional stream velocity u_{cr} above which the axial cylinder state loses its stability. Previous works have shown that cylinder motion sets in via divergence, while flutter appears as a secondary instability [10].

Setting the upstream end actuation to zero ($\Phi(t)\equiv\Psi(t)\equiv 0$ in (16)), and substituting a non-trivial eigensolution $\zeta(x_1,t)=z_\sigma(x_1)e^{i\sigma t}$ into (15) and (16), yield an eigenvalue problem for $\sigma=\sigma(l,u)$ and the eigenfunction $z_\sigma(x_1)$. The critical conditions for instability are obtained by setting the growth rate of perturbations ($\mathrm{Im}\{\sigma\}$) to zero and searching for parameter combinations satisfying the dispersion relation $\mathcal{D}(l,u;\mathrm{Re}\{\sigma\})=0$.

Fig. 2 presents the neutral curve obtained in the (l,u) plane for the above-specified choice of parameters. The shaded and unshaded zones mark the domains of stability ($\mathrm{Im}\{\sigma\}>0$) and instability ($\mathrm{Im}\{\sigma\}<0$), respectively. In agreement with previous analyses, our calculations show that instability sets in via divergence with $\mathrm{Re}\{\sigma\}=0$. At each value of the compression-length parameter l the figure depicts the critical value u_{cr} above which instability sets in. The critical dimensionless velocity decreases with l for $l\lesssim 2$, and remains nearly constant ($u_{cr}\approx 1.44$) for $l\gtrsim 2$, showing that critical conditions for instability in sufficiently 'long' cylinders are not affected by l. Also presented in Fig. 2 are the counterpart results of Ref. [10], marked by crosses (cf. their Fig. 3b). The close agreement between the two predictions supports the application of the present numerical scheme to study the system response to external excitation.

It should be noted that the numerical solution of Ref. [10] also predicts the occurrence of flutter instability as a secondary instability (of a Païdoussis type) at $u>u_{cr}$. However, for consistency with our preliminary assumption of small-amplitude cylinder motion, the following analysis of the forced motion is confined to cases where $u<u_{cr}$, so that all the eigenmodes of the unforced system are exponentially decaying with time, and the forced motion remains the only nontrivial system response. Nonlinear interactions between the unforced and forced cylinder motions are therefore ignored, and the small amplitude of cylinder deflection is ensured by prescribing small magnitudes of upstream end displacement (ε_d) and rotation (ε_r).

3.2. Forced motion

Focusing on the subcritical conditions $u<u_{cr}$ delineated in Fig. 2, we first consider the motion at $u\ll 1$ which is amenable to analytical solution. This motion can be considered as a limit case where the cylinder has large bending stiffness or is subject to low stream-flow velocity. We then study the general case of $u\sim O(1)<u_{cr}$, and examine the limits of validity of the $u\ll 1$ approximation.

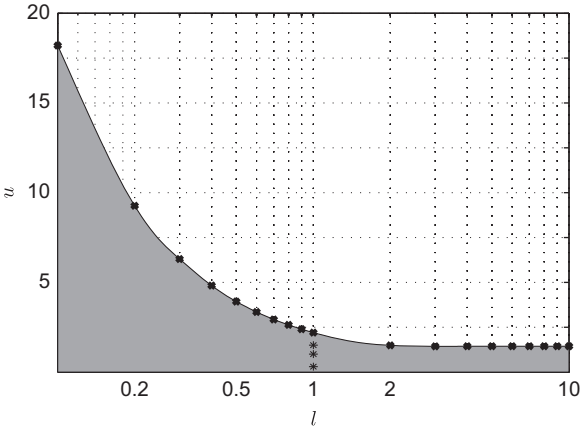

Fig. 2. The neutral curve in the (l,u) plane. The shaded and unshaded zones mark domains of stability and instability, respectively, and the crosses denote the results of Ref. [10]. Asterisks mark locus of points considered in Figs. 3–7 ($l=1$ and $u=0.3,1,1.5$).

3.2.1. The case $u \ll 1$

We expand the solution for $z(x_1)$ in (21) and (22) in powers of u and write

$$z(x_1) \approx z^{(0)}(x_1) + u z^{(1)}(x_1) + \cdots. \tag{25}$$

Substituting (25) into (21) and (22), and equating terms of the same order in u, we obtain a set of problems for $z^{(n)}$ $(n = 0, 1, \ldots)$. The equation for the leading order is

$$z^{(0)''''} - \omega^2 z^{(0)} = 0, \tag{26}$$

and the corresponding boundary conditions are

$$z^{(0)}(-l) = \varepsilon_d, \quad z^{(0)'}(-l) = \varepsilon_r e^{i\varphi}, \quad z^{(0)''}(0) = z^{(0)'''}(0) = 0. \tag{27}$$

This is equivalent to the problem for a clamped-free elastic beam set in vacuum and subject to sinusoidal actuation at $x_1 = -l$. The particular solution satisfying the boundary conditions is

$$z^{(0)}(x_1) = A_0[\cos(\sqrt{\omega}x_1) + \cosh(\sqrt{\omega}x_1)] + B_0[\sin(\sqrt{\omega}x_1) + \sinh(\sqrt{\omega}x_1)], \tag{28}$$

where

$$A_0 = \frac{\varepsilon_d[\cos(\sqrt{\omega}l) + \cosh(\sqrt{\omega}l)] + \varepsilon_r e^{i\varphi}[\sin(\sqrt{\omega}l) + \sinh(\sqrt{\omega}l)]/\sqrt{\omega}}{2[1 + \cos(\sqrt{\omega}l)\cosh(\sqrt{\omega}l)]},$$

$$B_0 = \frac{1}{\cos(\sqrt{\omega}l) + \cosh(\sqrt{\omega}l)}[\varepsilon_r e^{i\varphi}/\sqrt{\omega} - A_0(\sin(\sqrt{\omega}l) - \sinh(\sqrt{\omega}l))]. \tag{29}$$

For either upstream end displacement or rotation the *in vacuo* beam deflects as a *standing* wave (see (20)). The solution is singular at the *in vacuo* eigenvalues of a clamped-free unforced beam, satisfying

$$1 + \cos(\sqrt{\omega_{res}}l)\cosh(\sqrt{\omega_{res}}l) = 0, \tag{30}$$

and yielding the values $\sqrt{\omega_{res}}l \approx 1.86, 4.69, 7.85, \ldots$ [20]. At these eigenvalues a resonance motion occurs and the structure deflection becomes unbounded (see discussion at the end of this section).

The $O(u)$ problem for $z^{(1)}$ is governed by the equation

$$z^{(1)''''} - \omega^2 z^{(1)} = -2i\omega\sqrt{\mu}z^{(0)'} - i\omega\sqrt{\mu}\left(1 - \frac{1}{2}c_b\right)\frac{c_N}{c_T}z^{(0)}, \tag{31}$$

together with the boundary conditions

$$z^{(1)}(-l) = z^{(1)'}(-l) = z^{(1)''}(0) = 0, \quad z^{(1)'''}(0) = -i\omega f\sqrt{\mu}z^{(0)}(0). \tag{32}$$

The problem obtains the particular solution

$$z^{(1)}(x_1) = A_1[\cos(\sqrt{\omega}x_1) + \cosh(\sqrt{\omega}x_1)] + B_1\sin(\sqrt{\omega}x_1) + C_1\sinh(\sqrt{\omega}x_1) \tag{33}$$

$$+ \frac{x_1}{4\omega^{3/2}}[d_1\cos(\sqrt{\omega}x_1) + d_2\cosh(\sqrt{\omega}x_1) - d_3(\sin(\sqrt{\omega}x_1) - \sinh(\sqrt{\omega}x_1))], \tag{34}$$

where the constants d_1, d_2, d_3 are determined by satisfying the forcing term in (31), and A_1, B_1, C_1 are calculated using the boundary conditions (32), as described in Appendix A. Remarkably, all the constants obtained are pure imaginary, manifesting $z^{(1)}$ as a *propagating* wave correction over the leading order solution $z^{(0)}$. The effect of axial fluid flow is therefore to convect energy from the upstream edge driver to the downstream end. As a result, flow velocity has a damping effect on the otherwise singular behavior of the system close to its *in vacuo* resonance frequencies, as will be demonstrated in Section 3.2.2 and Fig. 3.

The asymptotic scheme for $u \ll 1$ can be continued indefinitely to higher $O(u^n)$ corrections. For a given nth order, the problem consists of an equation of the form

$$z^{(n)''''} - \omega^2 z^{(n)} = F(z^{(n-1)}, z^{(n-2)}),$$

together with boundary conditions

$$z^{(n)}(-l) = z^{(n)'}(-l) = z^{(n)''}(0) = 0, \quad z^{(n)'''}(0) = G(z^{(n-1)}, z^{(n-2)})$$

(where F and G are known functions of lower-order solutions), and can be solved in a closed form. Yet, for the purpose of qualitatively examining the effect of fluid flow, the present analysis is confined to calculation of the $O(u)$ correction.

According to the $u \ll 1$ approximation, excitation of the cylinder at one of the system *in vacuo* eigenfrequencies $\omega = \omega_{res}$ satisfying (30) yields an unbounded response. This singular behavior contradicts the small-amplitude assumption made at the outset, and the $u \ll 1$ solution therefore becomes invalid at $\omega = \omega_{res}$. Apart from the unboundedness of $z^{(0)}$, the expression (34) obtained for $z^{(1)}$ also diverges as $\omega \to \omega_{res}$, making the expansion (25) non-uniform. Yet, when the actuation amplitude (governed by ε_d and ε_r) is sufficiently small, the approximate solution should remain effective for $u \ll 1$ close to ω_{res}. In the following section, we turn to examine the $u \ll 1$ approximation by comparing it with a general

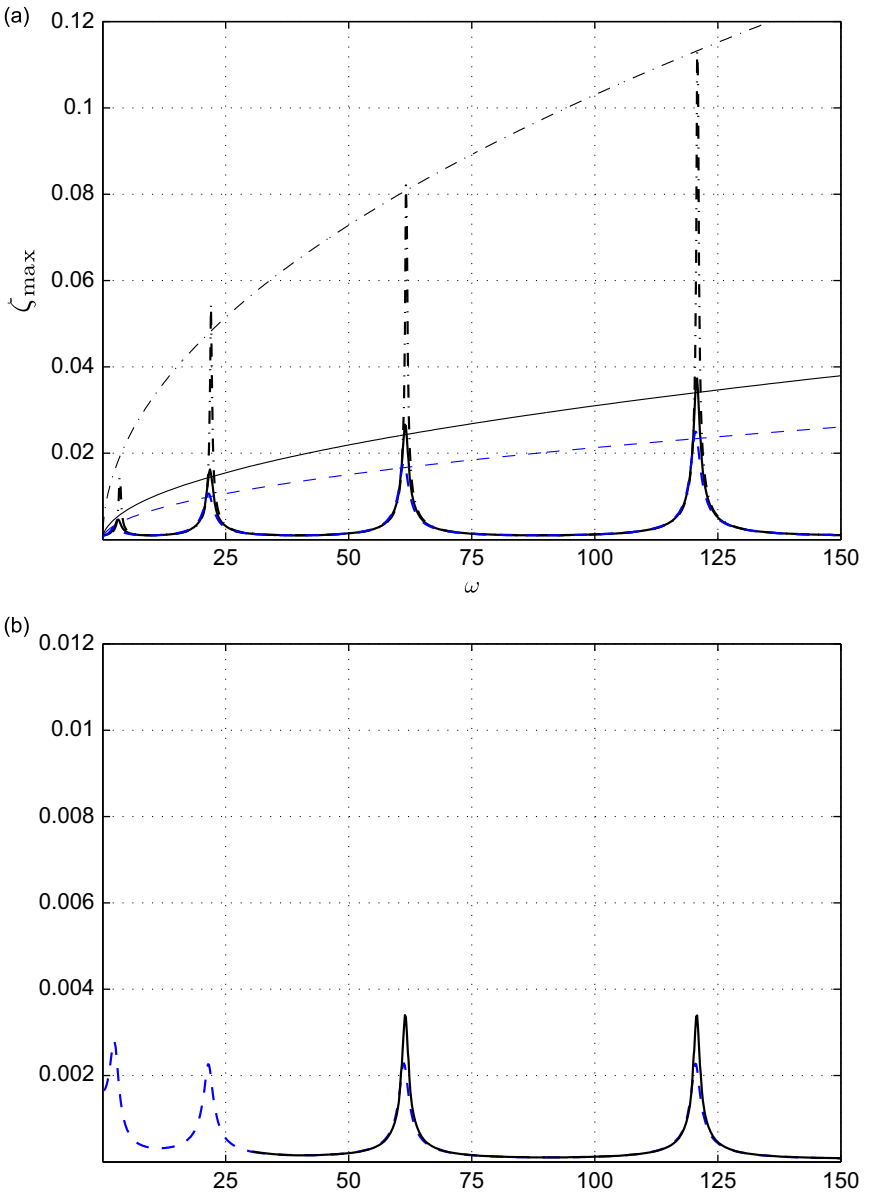

numerical solution for arbitrary $u \sim O(1)$ and ω. Separate qualitative analysis of the effect of fluid flow on the cylinder motion at $\omega = \omega_{res}$ will be presented in Fig. 3 and its discussion.

3.2.2. The case $u \sim O(1)$

From this point on, our results are presented for $l=1$, corresponding to a cylinder with $L_n = L$ (see (17)), thus equivalent to scaling the length by the cylinder length. Our calculations indicate that similar qualitative results are obtained for "shorter" ($l < 1$) and "longer" ($l > 1$) cylinders. The main quantitative effect of l on the results is in modifying the values of resonance eigenfrequencies, which are proportional l^{-2} (see (30) *et seq.*). Thus, "longer" cylinders resonate at lower frequencies, so that the product $\sqrt{\omega_{res}}l$ is kept unaltered. With other effects of l being minor, we omit further discussion on the impact of this parameter on the results.

According to Fig. 2, the critical nondimensional velocity for instability of the unforced cylinder at $l=1$ is $u_{cr} \approx 2.2$. Focusing on subcritical conditions, Fig. 3 presents the variation of the maximal cylinder deflection ζ_{max}, obtained during a period, with

actuation frequency, typically occurring at the cylinder downstream end, at three subcritical values of $u = 0.3,1$ and 1.5. The figure shows responses to actuations of displacement with no rotation (Fig. 3a) and rotation with no displacement (Fig. 3b). The results presented by the bold lines were obtained by exact numerical solution of the linearized problem (20)–(22).

Fig. 3a and b shows similar qualitative behavior, where large cylinder deflections are obtained close to the resonance frequencies $\omega_{res} \approx 3.45,22.0,61.6$ and 121 corresponding to $l=1$ (see (30)). With increasing u, the magnitude of deflections decays considerably, indicating the regularizing effect of fluid flow on the resonance behavior of the system. Remarkably, in the case of displacement actuation (Fig. 3a), the cylinder deflection at $\omega = \omega_{res}$ is increasing with ω_{res}, showing larger deflections at larger resonance frequencies. This trend is not observed in the case of rotation actuations (Fig. 3b), where the maximal cylinder deflection at ω_{res} appears unaffected by ω_{res}. In general, larger deflections are found in the case of upstream-end displacement (note the order of magnitude difference between the ζ_{max} scales in Fig. 3a and b).

To gain further insight into the increase in ζ_{max} with ω_{res} observed in Fig. 3a, we consider a simplified problem where the effect of stream-flow velocity is retained only in the free-end boundary condition. The analysis is described in Appendix B. While this model problem is not obtained as a rigorous limit of the full problem (22) and (23), it is amenable to analytical solution leading to qualitative description of the phenomena indicated above. The solution in Appendix B (see (B.4) and (B.6)) shows a square-root dependence of the maximum cylinder deflection on the resonance frequency in the case of displacement actuation

$$\xi_{max}(\omega_{res}) \approx \frac{1}{u}[K_d\sqrt{\omega_{res}}\varepsilon_d + K_r\varepsilon_r], \tag{35}$$

where K_d and K_r are constants of proportionality. The damping effect of stream-flow velocity is manifested through the inverse relation between ζ_{max} and u. These predictions are in close qualitative agreement with the exact numerical solution, as demonstrated by comparison between the bold and thin lines in Fig. 3a. It should be noted, however, that the value of K_d was not obtained through the qualitative analysis in Appendix B, but was found through numerical matching to fit the findings in Fig. 3a.

According to present linear theory we therefore find that the maximal cylinder deflection grows linearly with $\sqrt{\omega_{res}}$ for $\varepsilon_d \neq 0$. In reference to the case of no stream-flow velocity (in which unbounded resonance takes place for all $\omega = \omega_{res}$), we conclude that incoming flow has a stronger damping effect on the lower modes, and that the relatively low (subcritical) flow speeds considered are less efficient in damping displacement-induced motions at high frequencies. Interestingly, in the case of rotation actuation with no displacement ($\varepsilon_r \neq 0, \varepsilon_d = 0$), both Fig. 3b and the results in Appendix B (see (35)) indicate that the maximal cylinder deflection is unaffected by ω_{res}. Thus, the incoming flow in this case has uniform damping effect on all modes. In practice, of course, non-linear effects should become important at large enough stream-flow speeds or at large frequencies in the case of displacement actuation, and may act to lower the cylinder deflection. These effects, however, are beyond the scope of the present contribution.

To examine the time evolution of the cylinder shape, and compare between the numerical and the approximate $u \ll 1$ solutions, Fig. 4 presents the cylinder deflection at half-period ($t = t_p/2 = \pi/\omega$) and period ($t = t_p = 2\pi/\omega$) times, for a sinusoidally displaced cylinder with $u=1$ and $\varepsilon_d = 10^{-2}$ at various actuation frequencies. Both exact numerical solution (solid lines) and $u \ll 1$ approximation (dashed curves) are presented. The actuation frequencies in Fig. 4a–c are chosen distant from the resonance frequencies, while the forcing frequency $\omega = 21.5$ in Fig. 4d is close to the second resonance frequency $\omega_{res} \approx 22.0$ (see Fig. 3).

The geometrical shape of the cylinder in Fig. 4a–c is reminiscence of the first three eigenmodes of an elastic beam, where the cylinder intersects with the x_1-axis once (Fig. 4a), twice (Fig. 4b) and three times (Fig. 4c). The agreement between the numerical and approximate solutions is very good in all cases, which is remarkable in view of the relatively large value of $u=1$ depicted. The largest discrepancies appear in Fig. 4a close to the downstream end, and our calculations indicate that these differences completely disappear at a slightly lower u.

In contrast with Fig. 4a–c, relatively large discrepancies between the exact and approximate solutions appear in Fig. 4d, where $\omega = 21.5$. As discussed in Section 3.2.1, at the *in vacuo* eigenfrequency $\omega_{res} \approx 22.0$, the approximate solution becomes singular and cannot predict the system response. Yet, in the proximity of this frequency the $u \ll 1$ solution should still provide a reasonable approximation, given that u is sufficiently small. More specifically, for the $u \ll 1$ solution to be valid, u should be taken smaller when the actuation frequency is closer to ω_{res}. In Fig. 4d, the combination of an actuation frequency close to $\omega_{res} \approx 22.0$, together with the relatively large value of $u=1$, results in the considerable discrepancy between the approximate and exact solutions. Note that the typical value of cylinder deflection in this case is much larger (by an order of magnitude) than in Fig. 4a–c, in accordance with the 'near-resonance' behavior. In addition, unlike in Fig. 4a–c, the cylinder deflection at $t = t_p/2$ (attributed solely to the correction term $uz^{(1)}(x_1)$ in the $u \ll 1$ approximation; see Eqs. (21) and (26)) in Fig. 4d is similar in magnitude to that at $t = t_p$. This shows that the correction term in the approximate solution, representing the effect of fluid flow, is no longer small, and that the asymptotic expansion becomes non-uniform close to ω_{res}. We further elaborate on this point in the next section, where the far-field acoustic radiation of the cylinder is discussed.

3.3. Acoustic radiation

The approximate solution for $u \ll 1$ found in Section 3.2.1 can be applied to evaluate the far-field acoustic pressure. Substituting (25) together with (28) and (34) into (24) and carrying out the elementary integrations along the axial

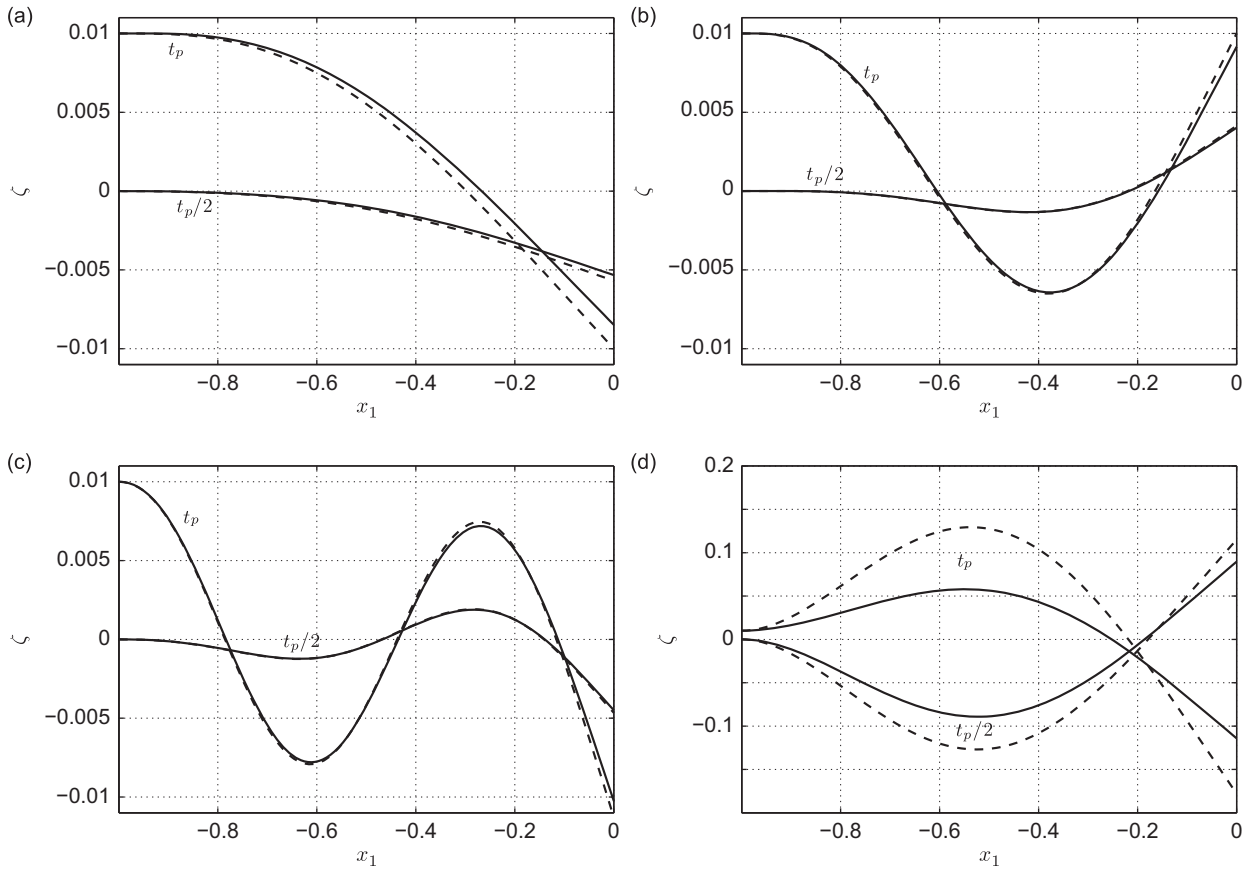

Fig. 4. Cylinder shapes at $l=1, u=1, \varepsilon_d=10^{-2}, \varepsilon_r=0$ and (a) $\omega=10$, (b) $\omega=40$, (c) $\omega=80$, (d) $\omega=21.5$. The solid lines mark the exact numerical solution and the dashed lines present the approximate solution for $u \ll 1$ (see Section 3.2.1) at the indicated values of time along a period, $t=t_p/2$ and $t=t_p$.

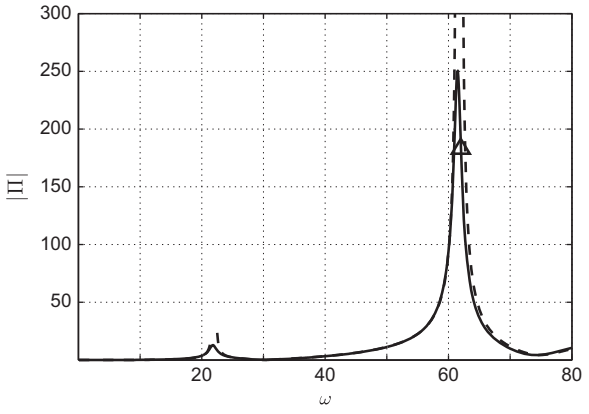

Fig. 5. Variation of magnitude of scaled acoustic pressure $|\Pi(\omega)|$ with actuation frequency for $l=1, u=1, \varepsilon_d=10^{-3}$ and $\varepsilon_r=0$. The solid line shows the exact numerical solution and the dashed line presents the approximate solution at $u \ll 1$ (see Section 3.2.1). The triangle marks the value of $|\Pi|$ considered as a reference value in Fig. 6a.

coordinate, yield an explicit expression for $\Pi(\omega)$, not given here for brevity. The validity of this approximation is examined below through comparison with the exact numerical solution for arbitrary $u \sim O(1)$.

Fig. 5 presents the variation of $|\Pi|$, the magnitude of scaled acoustic pressure (24), with actuation frequency, for $u=1, \varepsilon_d=10^{-3}$, and $\varepsilon_r=0$. The solid line shows the exact numerical solution and the dashed line marks the approximate solution for $u \ll 1$. The large values of $|\Pi|$ obtained do not contradict the linearization assumption, as the actual acoustic pressure is calculated by multiplying Π with the presumably small values of Mach number and $(a/L)^2$ (see (23)). The approximate solution is not plotted in the vicinities of the resonant frequencies (i.e., close to $\omega_{res} \approx 3.45, 22.0$ and 61.6),

where it diverges. The acoustic radiation shown in Fig. 5 is calculated at the same conditions as in the bold solid line in Fig. 3a, describing the dynamical response.

In accordance with the dynamical response, the acoustic pressure generated by the cylinder motion exhibits large values close to the *in vacuo* frequencies $\omega_{res} \approx 22.0$ and 61.6. Yet, the ratio between the two successive maxima of scaled pressure is substantially larger than that found in Fig. 3a. In addition, the exact numerical solution does not reflect resonance behavior (in the present scale of the *y*-axis) near the first *in vacuo* eigenfrequency, $\omega_{res} \approx 3.45$. These two results are mainly a consequence of the ω^3 factor multiplying the pressure signal (originating from the third time derivative of the cylinder position taken in the pressure calculation; see (18)), in addition to the square-root increase in the cylinder deflection discussed in Section 3.2.2 (see (35)), which magnify the predicted noise at large frequencies. Clearly, at large enough frequencies, non-linear effects should become important, and the high levels of acoustic pressure should be damped by higher-order mechanisms.

Comparison between the exact (solid line) and approximate $u \ll 1$ (dashed line) solutions in Fig. 5 shows very good agreement at frequencies that are sufficiently distant from the resonance frequencies. As in Fig. 4, this is particularly remarkable in view of the relatively large value of $u=1$ chosen. As expected from the discussion of the dynamical response, the agreement breaks down in the vicinity of ω_{res}, where the approximate solution diverges, while the exact numerical solution predicts finite values. The finite sound levels obtained, in contrast with the diverging behavior of the counterpart *in vacuo* setup, reflect the damping effect of fluid flow on both cylinder motion and acoustic radiation. At higher values of u this regularizing impact of the stream flow becomes even more pronounced. Physically, incoming flow causes the kinetic energy inserted into the system through upstream end actuation to convect into the fluid rather than cause diverging motion and sound levels as in the *in vacuo* problem. Yet, relatively high sound levels are obtained close to ω_{res}, and it is of interest to examine ways for controlling them, as suggested below.

Fig. 6 presents the effects of the ratio of actuation amplitudes $\varepsilon_r/\varepsilon_d$ (Fig. 6a), and phase shift angle φ (Fig. 6b), on the acoustic radiation, for $u=1, \varepsilon_d = 10^{-3}$ and $\omega = 62$. The results were obtained using the full numerical scheme, and the actuation frequency was chosen close to $\omega_{res} \approx 61.6$, so as to study how the relatively high sound level could be controlled. For reference, the value of $|\Pi|$ at the corresponding conditions of Fig. 5 ($\varepsilon_r/\varepsilon_d = 0$) is marked by a triangle in Figs. 5 and 6a.

According to Fig. 6a and b, both curves exhibit a minimum in $|\Pi|$ at some intermediate values of $\varepsilon_r/\varepsilon_d$ and φ, indicating that the sound level can be reduced by varying these parameters. In Fig. 6a, the acoustic pressure level forms a minimum at $\varepsilon_r/\varepsilon_d \approx 7.7$. In Fig. 6b, a minimum is obtained at $\varphi \approx \pi$, demonstrating that the acoustic radiation is minimized when displacement and rotation are applied at opposite phases. Quantitatively, the effect of $\varepsilon_r/\varepsilon_d$ on sound radiation appears more pronounced than that of φ, causing a reduction in $|\Pi|$ of up to $\approx 90\,\%$.

To rationalize these results, Fig. 7 presents the cylinder shape at the same parameter combination of $u=1$ and $\omega = 62$, and at time $t = t_p$, for two choices of the forcing parameters, $(\varepsilon_d, \varepsilon_r, \varphi) = (10^{-3}, 0, 0)$ (solid line), and $(\varepsilon_d, \varepsilon_r, \varphi) = (0, 10^{-3}, \pi)$ (dashed line). The result in Fig. 6a can be rationalized by taking the linear superposition of the dashed line (showing the deflection resulting from rotation with $\varphi = \pi$) multiplied by $\varepsilon_r/\varepsilon_d$, and the solid line (showing the deflection caused by displacement) in Fig. 7: when $\varepsilon_r/\varepsilon_d \lesssim 7.7$, the rotation-induced motion acts to reduce the deflection and sound production due to upstream-end displacement; however, for $\varepsilon_r/\varepsilon_d \gtrsim 7.7$, the contribution of rotation "overcomes" the opposite-phase effect of displacement and becomes dominant. Our calculations indicate that the occurrence of this minimum at some intermediate value of $\varepsilon_r/\varepsilon_d$ takes place in situations where the phase φ between rotation and displacement actuations is nonzero. The value of $\varepsilon_r/\varepsilon_d$ which minimizes the sound for given $\varphi \neq 0$ varies with φ, and may be a useful mean for controlling the acoustic radiation of the cylinder. The reduction of the acoustic pressure is most efficient in the case $\varphi = \pi$ presented.

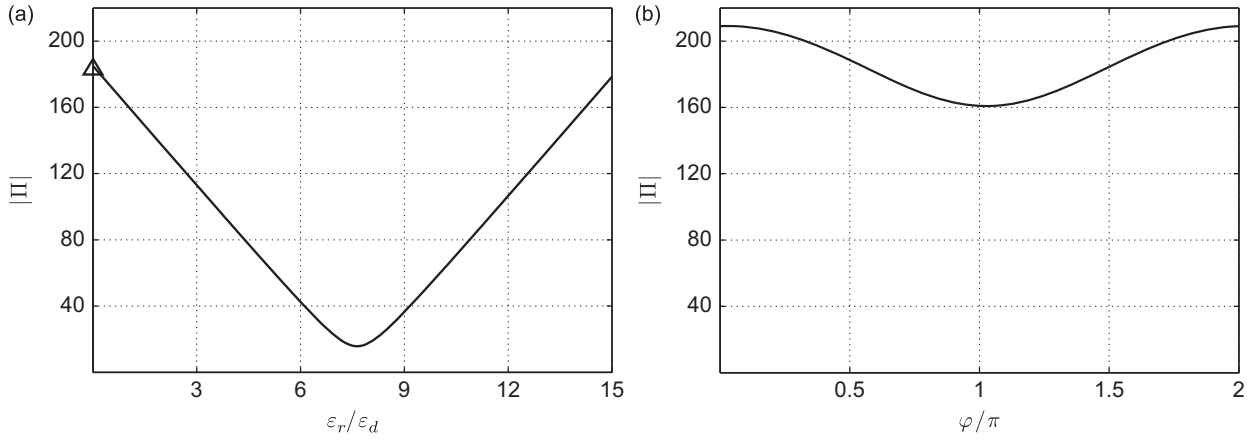

Fig. 6. Variation of magnitude of scaled acoustic pressure $|\Pi(\omega)|$ with (a) ratio of actuation amplitudes $\varepsilon_r/\varepsilon_d$, and (b) phase angle φ. In both cases, $l=1, u=1, \omega=62$ and $\varepsilon_d = 10^{-3}$. In Fig. 6a, $\varphi = \pi$, and in Fig. 6b, $\varepsilon_r = 10^{-3}$. The triangle in Fig. 6a at $\varepsilon_r/\varepsilon_d = 0$ marks the value of $|\Pi|$ at conditions of Fig. 5.

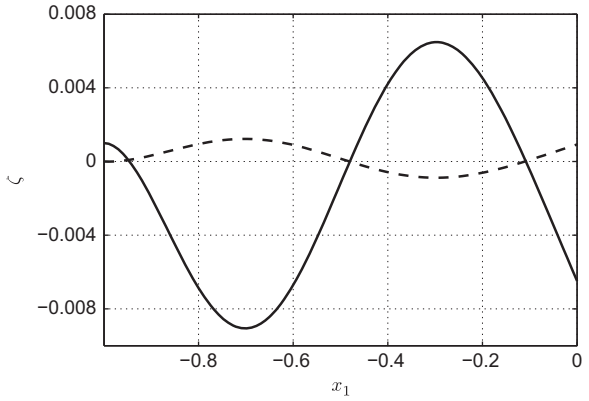

Fig. 7. Cylinder shape at time $t = t_p$ for $l = 1, u = 1$ and $\omega = 62$ for $(\varepsilon_d, \varepsilon_r, \varphi) = (10^{-3}, 0, 0)$ (solid line) and $(\varepsilon_d, \varepsilon_r, \varphi) = (0, 10^{-3}, \pi)$ (dashed line).

Similarly, Fig. 7 can be used to explain the results in Fig. 6b. The effect of φ on $|\Pi|$ for $\varepsilon_r/\varepsilon_d = 1$ can be obtained by multiplying the dashed line in Fig. 7 with a proper phase with respect to the solid line and taking their linear superposition. At the out-of-phase ($\varphi = \pi$) conditions presented in Fig. 7, it can be seen that the two signals are in opposite directions (and intersecting at $\zeta = 0$), thus leading to the minimum found in Fig. 6b. At other values of φ, this cancelation mechanism becomes less efficient and replaced by partial adding of the two signals along some sections of the cylinder. In particular, when the two actuations act in phase ($\varphi = 0$), the rotation-induced signal is given by the negative sign of the dashed line in Fig. 7. In contrast with the $\varphi = \pi$ case, this signal now adds to the displacement-induced contribution, and the total deflection and subsequent sound radiation are amplified.

4. Conclusion

We studied the linearized motion and far-field sound generated by an elastic cylinder subject to uniform axial flow and harmonic upstream-end actuation. The actuation input was combined of sinusoidal displacement and rotation with a common frequency, and can be viewed as a Fourier component of the system response to a more general, and possibly non-periodic, actuation. The analysis of the far-field acoustic pressure relied on the assumption of cylinder compactness, thus confined to small-enough actuation frequencies (see discussion in Section 2.2).

Throughout our analysis, the generation of vorticity at the structure boundary and its transmission into sound were excluded. This was allowed by considering a cylinder with a well-streamlined downstream edge (controlled by the parameter f introduced in (9)) and by focusing on a linearized regime of low stream-flow velocities, considerably below the critical velocity for cylinder instability. Generally, vortex shedding may occur at the structure upstream or downstream ends. The negligence of upstream-end shedding is common to other studies considering the motion of a thin elastic plate actuated at its leading edge (e.g., Refs. [11,12,15]), and is justified through the small amplitudes of motion applied at this point, as in our setup. Yet, at the structure trailing edge satisfaction of the Kutta condition necessitates release of trailing edge vortices. The strength of trailing edge vorticity is regularly proportional to the size of the trailing edge. In the present setup of a well-streamlined cylinder, the cylinder cross section reduces smoothly and gradually to a downstream end of negligible area, thus allowing for the negligence of trailing edge vortex shedding. In practice, when flow detachments take place, or when the cylinder interacts with incident turbulence, the effect of vorticity as a source of sound may become important and should be taken into account [15,18]. Particularly, when the cylinder is blunt (corresponding to the case $f=0$), it is nevertheless possible that the effect of vortex shedding on the far field sound becomes dominant. We are not familiar with any existing studies modeling the vorticity field generated by an elastic cylinder in axial flow, which may suggest this topic as a subject for future examination, primarily in the context of acoustic radiation evaluation.

In accordance with the linearity assumption made at the outset, the analysis of the forced motion has focused on subcritical conditions where the unforced cylinder is aligned with the incoming flow. Under such conditions of relatively low stream velocities (or large bending stiffness), the dynamics of the system is considerably affected by the *in vacuo* properties of the cylinder, characterized by resonance motion of the structure when actuated at one of its *in vacuo* eigenfrequencies ω_{res}. The effect of fluid flow is nevertheless crucial in convecting this singularity and transferring it into kinetic energy in the fluid, thus reducing both cylinder deflection and acoustic radiation in the vicinity of ω_{res}. An analytic approximation was obtained, which captured the leading order effect of fluid flow on the system, both at and in the vicinity of the system *in vacuo* eigenfrequencies. It was shown that fluid flow is more efficient in regularizing the resonance system response at lower frequencies in the case of displacement actuation, while all modes are equally damped when rotation actuation is applied. Finally, it was demonstrated how the system dynamic and acoustic behaviors can be controlled through the variation of the actuation parameters.

Dowling [7] considered the forced motion of an elastic cylinder displaced harmonically at its upstream end. Her analysis focused on a case where the bending rigidity of the structure is infinitely small. In terms of the present

nondimensional formulation, this refers to a situation where the nondimensional velocity is very large ($u \gg 1$). It was shown that in this asymptotic limit, when cylinder divergence is excluded at the outset, the system is always stable to small perturbations. Thus, non-linear interactions between unforced and forced cylinder responses were not considered. As later shown in Ref. [10], when the cylinder bending rigidity is finite, system instability takes place via divergence (see Fig. 2 and its discussion), which evolves into flutter at supercritical conditions. The present work considers the forced system behavior at $u \lesssim O(1)$; it can therefore be considered complementary to the analyses of Refs. [7,10], by studying the forced system response at subcritical conditions, where the cylinder bending rigidity is relatively large. A separate investigation should aim at addressing the non-linear problem at supercritical flow velocities.

Acknowledgements

This work was supported by the Marie Curie International Reintegration Grant no. PIRG-GA-2010-276837.

Appendix A. Determination of the coefficients in (34)

The A_1,B_1 and C_1 terms in (34) compose the homogeneous solution of (31). Substituting (34) into (31) and equating the coefficients from both sides of the equation yield a system of linear equations for d_1,d_2 and d_3, solved by

$$d_1 = -k_1 A_0\sqrt{\omega} + k_2 B_0, \quad d_2 = k_1 A_0\sqrt{\omega} + k_2 B_0, \quad d_3 = k_2 A_0 + k_1 B_0\sqrt{\omega}, \tag{A.1}$$

with

$$k_1 = -2i\omega\sqrt{\mu}, \quad k_2 = -i\omega\sqrt{\mu}\left(1-\frac{1}{2}c_b\right)\frac{c_N}{c_T}. \tag{A.2}$$

To specify A_1,B_1 and C_1, note that the form (34) satisfies the boundary condition $z^{(1)''}(0) = 0$ in (32) automatically. Imposing the other three boundary conditions in (32) yields a system of equations

$$A_1[\cos(\sqrt{\omega}l)+\cosh(\sqrt{\omega}l)] - B_1\sin(\sqrt{\omega}l) - C_1\sinh(\sqrt{\omega}l) = \frac{l}{4\omega^{3/2}}[d_1\cos(\sqrt{\omega}l) + d_2\cosh(\sqrt{\omega}l) + d_3(\sin(\sqrt{\omega}l)-\sinh(\sqrt{\omega}l))], \tag{A.3}$$

$$\begin{aligned} A_1[\sin(\sqrt{\omega}l)-\sinh(\sqrt{\omega}l)] + B_1\cos(\sqrt{\omega}l) + C_1\cosh(\sqrt{\omega}l) = \frac{1}{4\omega^2}\{&-d_1\cos(\sqrt{\omega}l) - d_2\cosh(\sqrt{\omega}l) - d_3(\sin(\sqrt{\omega}l)-\sinh(\sqrt{\omega}l)) \\ &+\sqrt{\omega}l[d_1\sin(\sqrt{\omega}l) - d_2\sinh(\sqrt{\omega}l) - d_3(\cos(\sqrt{\omega}l)-\cosh(\sqrt{\omega}l))]\}, \end{aligned} \tag{A.4}$$

and

$$-\omega^{3/2}B_1 + \omega^{3/2}C_1 = \frac{3}{4\omega^{1/2}}(d_1-d_2) + 2A_0k_3, \tag{A.5}$$

where

$$k_3 = -i\omega f\sqrt{\mu}. \tag{A.6}$$

Explicit expressions for A_1,B_1 and C_1 obtained from solution of (A.3)–(A.5)) are not presented here for brevity.

Appendix B. Qualitative evaluation of ζ_{max} at $\omega = \omega_{res}$

To consider the effect of non-zero stream flow velocity on the maximum (free-end) cylinder deflection at the *in vacuo* frequencies, consider a simplified case where the $u \neq 0$ term is retained only in the *f*-term of the free-end boundary conditions in (21) and (22). Thus, we seek for a solution for the equation

$$z''' - \omega^2 z = 0, \tag{B.1}$$

in conjunction with the boundary conditions

$$z(-l) = \varepsilon_d, \quad z(-l) = \varepsilon_r e^{i\varphi} \quad z''(0) = 0, \quad z'''(0) + i\omega f u\sqrt{\mu}z(0) = 0. \tag{B.2}$$

It should be noted that (B.1) and (B.2) are not obtained as a rigorous asymptotic limit of (21) and (22) and are therefore not expected to yield a quantitative approximation for the general solution of the problem at $\omega = \omega_{res}$. However, as demonstrated by comparison with the results in Fig. 3, this simplified model supplies qualitative insight into the impact of incoming stream flow on the system behavior at its *in vacuo* resonance frequencies.

The solution of (B.1) satisfying the condition $z''(0) = 0$ is

$$z(x_1) = A[\cos(\sqrt{\omega}x_1)+\cosh(\sqrt{\omega}x_1)] + B\sin(\sqrt{\omega}x_1) + C\sinh(\sqrt{\omega}x_1). \tag{B.3}$$

Focusing on the maximum cylinder deflection (see (20))

$$\zeta_{max} = \max\{z(0)e^{i\omega t}\} = \max\{2Ae^{i\omega t}\}, \tag{B.4}$$

and applying the remaining three boundary conditions in (B.2) to obtain the value of A, we find

$$\mathrm{A}(\omega)=\left[-\frac{2\mathrm{i}}{\sqrt{\omega}}\mathrm{f_u}\sqrt{\mu}\,\sin(\sqrt{\omega}\mathrm{l})+\frac{2\Delta(\omega)\sin(\sqrt{\omega}\mathrm{l})}{\sin(\sqrt{\omega}\mathrm{l})\cosh(\sqrt{\omega}\mathrm{l}))-\cos(\sqrt{\omega}\mathrm{l})\sinh(\sqrt{\omega}\mathrm{l})}\right]^{-1}$$
$$\times\left[\varepsilon_{\mathrm{d}}+\frac{\varepsilon_{\mathrm{d}}\cos(\sqrt{\omega}\mathrm{l})+\varepsilon_{\mathrm{r}}\mathrm{e}^{\mathrm{i}\varphi}\sin(\sqrt{\omega}\mathrm{l})/\sqrt{\omega}}{\sin(\sqrt{\omega}\mathrm{l})\cosh(\sqrt{\omega}\mathrm{l})-\cos(\sqrt{\omega}\mathrm{l})\sinh(\sqrt{\omega}\mathrm{l})}(\sin(\sqrt{\omega}\mathrm{l})+\sinh(\sqrt{\omega}\mathrm{l}))\right],\tag{B.5}$$

where $\Delta=1+\cos(\sqrt{\omega}\mathrm{l})\cosh(\sqrt{\omega}\mathrm{l})$. At $\omega=\omega_{\mathrm{res}}$, $\Delta=0$ (see (30)). Evidently, it is then only the first term on the RHS of (B.5), originating from the u-term retained in the boundary conditions (B.2), which regularizes $\mathrm{A}(\omega)$ and prohibits unbounded resonance. Taking the limit $\sqrt{\omega_{\mathrm{res}}}\mathrm{l}\gg 1$ (valid from the third to higher resonance frequencies; see (30) *et seq.*), we obtain

$$\mathrm{A}(\omega_{\mathrm{res}})\approx\frac{\mathrm{i}}{2\mathrm{f_u}\sqrt{\mu}}($$